

# *Ab initio* Full Cell $GW+DMFT$ for Correlated Materials

Tianyu Zhu\* and Garnet Kin-Lic Chan†

Division of Chemistry and Chemical Engineering, California Institute of Technology, Pasadena CA 91125

The quantitative prediction of electronic properties in correlated materials requires simulations without empirical truncations and parameters. We present a method to achieve this goal through a new *ab initio* formulation of dynamical mean-field theory (DMFT). Instead of using small impurities defined in a low-energy subspace, which require complicated downfolded interactions which are often approximated, we describe a full cell  $GW+DMFT$  approach, where the impurities comprise all atoms in a unit cell or supercell of the crystal. Our formulation results in large impurity problems, which we treat here with efficient quantum chemistry impurity solvers that work on the real-frequency axis, combined with a one-shot  $G_0W_0$  treatment of long-range interactions. We apply our full cell approach to bulk Si, two antiferromagnetic correlated insulators NiO and  $\alpha\text{-Fe}_2\text{O}_3$ , and the paramagnetic correlated metal  $\text{SrMoO}_3$ , with impurities containing up to 10 atoms and 124 orbitals. We find that spectral properties, magnetic moments, and two-particle spin correlation functions are obtained in good agreement with experiment. In addition, in the metal oxide insulators, the balanced treatment of correlations involving all orbitals in the cell leads to new insights into the orbital character around the insulating gap.

## I. INTRODUCTION

Computing the properties of correlated electron materials with quantitative accuracy remains a fundamental challenge in *ab initio* simulations [1]. This is because strong electron interactions, for example in materials with open  $d$  or  $f$  shells, can lead to emergent phases such as high-temperature superconductivity, which cannot be described by the mean-field and low-order perturbation approximations commonly employed by *ab initio* methods.

Quantum embedding methods [2–5] in principle provide a promising route to access the phase diagrams of correlated materials, because they simultaneously treat strong local electron interactions and the thermodynamic limit. Among the different variants of quantum embedding used for this purpose, the combination of dynamical mean-field theory (DMFT) (and its cluster extensions [6, 7]) and density functional theory (DFT) [8], known as DFT+DMFT, is very popular [9–11]. In this combination, one views DFT as a low-level theory that accounts for band structure and the long-range interactions, while the high-level solution of the DMFT impurity problem, defined on a small set of correlated orbitals, introduces diagrams arising from the strong local interactions. Yet despite many successes, DFT+DMFT does not provide a truly parameter-free and quantitative *ab initio* theory of correlated materials, due to two closely related issues. First, the local Coulomb interaction in the DMFT impurity problem is typically treated as an adjustable Hubbard-like parameter [12], or is else estimated within another approximation [13]. Second, a double-counting correction [14, 15] is required to remove the DFT contribution to the local interactions, but no consistently accurate double-counting correction is known [16]. Beyond these two primary concerns arising from the local interactions, density functionals also do not always reliably account for the long-range interaction effects [17].

To obtain a truly quantitative, *ab initio* formulation of

DMFT, one must work within a diagrammatically clean formalism. In this context, it is natural to replace DFT with the  $GW$  approximation [18] as the low-level theory. The  $GW$  approximation (often employed in its one-shot form ( $G_0W_0$ )) [19, 20] has been shown to fix many of the problems with semilocal density functionals (such as the underestimation of band gaps of weakly-correlated semiconductors) and thus appears a practical way to include the most important low-order long-range interaction diagrams. The combination with DMFT can then be formulated without double-counting by exactly subtracting the local  $GW$  contributions. The idea of self-consistently embedding the impurity self-energy and contributions to the polarization propagator arising from long-range interactions was proposed almost 18 years ago as the  $GW+(E)DMFT$  approximation [21, 22], but only very recently have self-consistent implementations appeared [23, 24]. However, while these developments are promising, applications have remained more limited than those with DFT+DMFT and have retained some problematic issues of that approach [25–30]. In particular, all current  $GW+(E)DMFT$  methods still require strongly downfolded interactions, because the impurity is restricted to the truncated low-energy subspace of a few correlated  $d$  or  $f$  orbitals (Fig. 1(b)). Downfolding to a small number of strongly coupled orbitals is numerically challenging, and yields retarded interactions that either limit the applicable impurity solvers or which must be truncated or otherwise approximated. If one ignores the embedding of the polarization propagator to work purely with the bare interactions, one obtains the self-energy embedding theory (SEET) [31]. However, applications of this simpler approach in realistic solids have only appeared very recently [32]. Aside from these technical issues, in some more complex correlated materials, the local orbitals can be intertwined with other itinerant bands [33, 34]. In such cases, even defining a set of local correlated orbitals can be difficult, and the quality of the calculation then depends sensitively on this choice [35].

A common origin of many of the above challenges is the definition of the impurity problem in terms of a small low-energy subspace. This is done only to obtain as simple an impurity problem as possible, as motivated by model Hamiltonians, but it is not a requirement of the more general DMFT

\* tyzhu@caltech.edu

† gkc1000@gmail.com

formalism. Consequently, in this work, we present a new formulation, which we term *ab initio* full cell *GW*+DMFT. In this approach we define the impurity to be the full unit cell - or even multiple unit cells of atoms - where each atom is described by a large localized set of atomic orbitals, covering the core, valence and high-energy virtual orbitals (Fig. 1(a)). Since no low-energy subspace is identified, there is no downfolding and its associated uncertainties, and we can simply use the full set of bare Coulomb interactions between the impurity orbitals, avoiding theoretical and numerical ambiguities. (A related full cell idea has been used to enable *GW*-in-DFT Green's function embedding [36]). In addition, important medium range (non-local) interaction effects, weaker than the strongest local correlations, but stronger than the interactions captured by *GW*, can now enter the theory. (Such interactions, which are neglected in standard *GW*+DMFT treatments, are known to yield significant errors in a variety of settings, for example in the treatment of metallic sodium [24]). While conceptually simple, our full cell approach engenders two new technical complexities. The first is the need to set up the large impurity problem (for example to efficiently generate all the matrix elements) but this is enabled by technical advances we have made in the PySCF simulation platform [37] and our recently developed general *ab initio* quantum embedding framework [38, 39]. The second is the need to solve the resulting impurity problem with a large number of orbitals. Here, the key insight is that many orbitals in the full cell impurity are only weakly correlated, and impurity solvers which take advantage of this, such as those used in molecular quantum chemistry [40, 41] can then work very efficiently. In this work, we will use two such kinds of solvers: a coupled-cluster singles and doubles (CCSD) Green's function solver [42, 43] as well as a selected configuration interaction (selected CI) solver [44], carrying out self-consistency along the real-frequency axis. The accuracy of such solvers in impurity problems has been benchmarked elsewhere [41, 42, 45, 46]: thus we emphasize that a specific choice of the solver is not the message of this work. Rather, our focus is on establishing a generic full cell embedding framework that avoids downfolding and introduces new non-local physics at two levels of approximation at medium and large distances, and whose mathematical formulation allows a natural combination with a wide variety of quantum chemistry impurity solvers, including the two used here. We apply the full cell *GW*+DMFT method to compute the spectral properties of Si, the spectra, magnetic moments and spin correlation functions of two correlated insulators, NiO and  $\alpha$ -Fe<sub>2</sub>O<sub>3</sub>, in their antiferromagnetic (AFM) phases, as well as the spectra of a paramagnetic correlated metal SrMoO<sub>3</sub>. Our largest calculation in hematite uses an impurity of four Fe and six O atoms, giving rise to an unprecedentedly large *ab initio* DMFT impurity problem with 124 impurity orbitals.

## II. THEORY AND IMPLEMENTATION

In the full cell *GW*+DMFT formulation, because the impurity cell contains all atoms in a crystal cell (or, more usually, a supercell), the effects of what would normally be thought

of as long-range interactions on the polarization and self-energy from within the supercell are all included. Also, because the supercell is treated at a level beyond *GW*, we include the medium-range interactions that are neglected in standard *GW*+DMFT treatments. However, we will treat contributions from long-range interactions beyond the supercell only at the level of the self-energy matrix of the crystal, computed at the one-shot  $G_0W_0$  level. Because of this, certain contributions to the polarization propagator involving interactions far from the supercell, that would require the bosonic self-consistency of EDMFT [24], are omitted. In practice, this means that rather than partitioning into the strictly strongest interactions (for example in a *d*- or *f*-shell), coupled to a low-level treatment of everything else as in standard *GW*+DMFT, our formulation prioritizes a higher-level treatment of interactions within a significant distance of the most correlated orbitals. The magnitude of the neglected effects from the lack of bosonic self-consistency, while ameliorated by the explicit treatment of large cells, can only be established through numerical experiments, as performed below. (An example of a case where the lack of bosonic self-consistency could be qualitatively important is in systems where there is an overlap of plasmon satellites and Hubbard bands [23]).

Given a periodic crystal, we start by performing a one-shot  $G_0W_0$  calculation on top of a mean-field reference (DFT or HF), using crystalline Gaussian atomic orbitals and Gaussian density fitting (GDF) integrals [47]. Because the  $G_0W_0$  approximation is reference dependent, we will denote the approximation  $G_0W_0@reference$ . The full  $G_0W_0$  self-energy matrix is computed in the mean-field molecular orbital (MO) basis along the imaginary-frequency axis [48, 49]:

$$\Sigma_{nn'}^{GW}(\mathbf{k}, i\omega) = -\frac{1}{2\pi} \sum_{m\mathbf{k}_m} \int_{-\infty}^{\infty} d\omega' [\mathbf{G}_0(\mathbf{k}_m, i\omega - i\omega')]_{mm} \times \sum_{PQ\mathbf{k}_p} v_P^{nm} [\mathbf{I} - \mathbf{\Pi}(\mathbf{k}_p, i\omega')]_{PQ}^{-1} v_Q^{mn'}, \quad (1)$$

where  $v_P^{nm}$  represents the 3-index electron repulsion integral (ERI)  $(P\mathbf{k}_p|n\mathbf{k}_nm\mathbf{k}_m)$ ,  $P$  is the Gaussian auxiliary basis, and  $n$  and  $m$  represent mean-field molecular orbitals (bands).  $\mathbf{k}_p$ ,  $\mathbf{k}_n$  and  $\mathbf{k}_m$  satisfy crystal momentum conservation:  $\mathbf{k}_p = \mathbf{k}_n - \mathbf{k}_m + n\mathbf{b}$ , where  $\mathbf{b}$  is a lattice vector, and  $\mathbf{G}_0(\mathbf{k}_m, i\omega - i\omega')$  is the mean-field Green's function. The integration in Eq. 1 is carried out efficiently using a modified Gauss-Legendre grid [48] (100 grid points were used in this study). The polarization kernel  $\mathbf{\Pi}(\mathbf{k}_p, i\omega')$  is

$$\mathbf{\Pi}_{PQ}(\mathbf{k}_p, i\omega') = 2 \sum_{i\mathbf{k}_i}^{\text{occ}} \sum_{a\mathbf{k}_a}^{\text{vir}} v_P^{ia} \frac{\epsilon_{i\mathbf{k}_i} - \epsilon_{a\mathbf{k}_a}}{\omega'^2 + (\epsilon_{i\mathbf{k}_i} - \epsilon_{a\mathbf{k}_a})^2} v_Q^{ai}, \quad (2)$$

where  $\epsilon_{i\mathbf{k}_i}$  and  $\epsilon_{a\mathbf{k}_a}$  are occupied and virtual orbital energies respectively. Note that in a Gaussian basis formulation, the number of bands and size of auxiliary basis are significantly smaller than in plane-wave *GW* formulations [50], and because of this, the summations in Eqs. 1-2 run over all bands. To obtain the real-frequency  $G_0W_0$  self-energy, we perform analytic continuation. Here, we fit the self-energy matrix elements to  $N$ -point Padé approximants ( $N = 18$  in this work)

using Thiele's reciprocal difference method [51]. For the detailed  $G_0W_0$  algorithm, we refer readers to Ref. [52]. Our  $G_0W_0$  scheme thus allows us to use continuation to obtain the retarded self-energy on the real axis at arbitrary broadenings, although as an alternative, a contour deformation scheme [53] may also be used to directly compute the real-frequency time-ordered self-energy without the need for analytic continuation. This latter strategy may be attractive to explore in the future to completely avoid possibly unstable analytic continuations.

To define the impurity problem, we first construct an orthogonal atom-centered local orbital (LO) basis. As in our previous work on *ab initio* HF+DMFT and density matrix embedding theory (DMET), we employ crystalline intrinsic atomic orbitals (IAOs) and projected atomic orbitals (PAOs) as the local orthogonal basis [38, 39, 54]. IAOs are a set of valence atomic-like orbitals that exactly span the occupied space of the mean-field calculations, whose construction only requires projecting the DFT/HF orbitals onto predefined valence (minimal) AOs. PAOs, on the other hand, provide the remaining high-energy virtual atomic-like orbitals that complete the atomic basis and capture the correlation and screening effects.

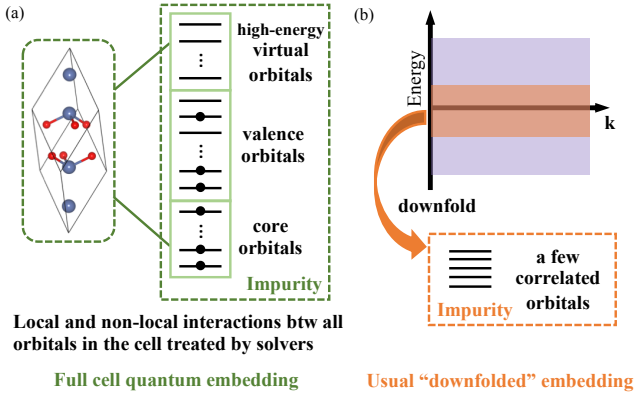


FIG. 1. Illustration of (a) *ab initio* full cell GW+DMFT and (b) usual GW+DMFT schemes. In full cell embedding, all orbitals in the full unit cell (four Fe and six O atoms) are taken as the impurity in the  $\alpha$ -Fe<sub>2</sub>O<sub>3</sub> calculation. In contrast, other GW+DMFT formulations define the impurity problem to contain a few correlated orbitals within a low-energy subspace which interact via downfolded, retarded, interactions.

The impurity consists of all LOs (i.e. all IAOs and PAOs) within the impurity cell (crystal cell or supercell) with IAOs representing the core and valence orbitals and PAOs representing the high-energy virtual orbitals. This is illustrated in Fig. 1(a). The most expensive step in forming the impurity Hamiltonian is computing the bare Coulomb interaction matrix  $(ij|kl)$  for all orbitals within the impurity cell. However, using Gaussian density fitting, we can do this at relatively low cost (scaling asymptotically as  $\mathcal{O}(N_{\mathbf{k}}^2 N_L N_{\text{AO}}^3)$ , where  $N_{\mathbf{k}}$ ,  $N_L$  and  $N_{\text{AO}}$  are the numbers of  $\mathbf{k}$  points and auxiliary Gaussian and atomic orbitals within the impurity cell). We refer readers to Ref. [39] for a detailed algorithm. The impurity Hamilto-

nian (without bath orbitals) is therefore

$$\hat{H}_{\text{imp}} = \sum_{ij \in \text{imp}} \tilde{F}_{ij} a_i^\dagger a_j + \frac{1}{2} \sum_{ijkl \in \text{imp}} (ij|kl) a_i^\dagger a_k^\dagger a_l a_j, \quad (3)$$

with the one-particle interaction  $\tilde{F}_{ij}$  defined as the Hartree-Fock effective Hamiltonian with the double-counting term subtracted

$$\tilde{F}_{ij} = (F_{\text{imp}})_{ij} - \sum_{kl \in \text{imp}} (\gamma_{\text{imp}})_{kl} [(ij|lk) - \frac{1}{2}(ik|lj)], \quad (4)$$

and with  $\gamma_{\text{imp}}$  as the impurity block of the mean-field density matrix.

We then start the DMFT cycle with an initial guess of the impurity self-energy as the  $G_0W_0$  local self-energy:  $\Sigma_{\text{imp}}(\omega) = \Sigma_{\text{DC}}^{GW}(\omega)$ . The  $G_0W_0$  local self-energy is computed in the LO basis within the impurity cell:

$$[\Sigma_{\text{DC}}^{GW}(i\omega)]_{ij} = -\frac{1}{2\pi} \sum_{kl} \int_{-\infty}^{\infty} d\omega' [\mathbf{G}_0^{\text{imp}}(i\omega - i\omega')]_{kl} \times \sum_{RS} L_R^{ik} [\mathbf{I} - \mathbf{\Pi}(i\omega')]_{RS}^{-1} L_S^{lj}, \quad (5)$$

and analytically continued to the real axis. Here, all local orbital indices  $(i, j, k, l)$  are within the impurity cell. The 3-index tensor  $L_R^{ij}$  is computed from a Cholesky decomposition of the impurity ERI:  $(ij|kl) = \sum_R L_R^{ij} L_R^{kl}$ . Note that the polarization propagator is computed in the impurity orbital space, first in the imaginary time domain [55, 56]:

$$\mathbf{\Pi}_{RS}(\tau) = \sum_{ijkl \in \text{imp}} L_P^{ij} [\mathbf{G}_0^{\text{imp}}(\tau)]_{ki} L_Q^{kl} [\mathbf{G}_0^{\text{imp}}(-\tau)]_{lj}, \quad (6)$$

and then cosine transformed into imaginary frequency space.

The hybridization self-energy is then computed:

$$\Delta(\omega) = (\omega + \mu)\mathbf{I} - \tilde{\mathbf{F}} - \Sigma_{\text{imp}}(\omega) - \mathbf{G}^{-1}(\mathbf{R} = \mathbf{0}, \omega), \quad (7)$$

with the lattice Green's function defined as

$$\mathbf{G}(\mathbf{R} = \mathbf{0}, \omega) = \frac{1}{N_{\mathbf{k}}} \sum_{\mathbf{k}} [(\omega + \mu)\mathbf{I} - \mathbf{h}(\mathbf{k}) - \Sigma(\mathbf{k}, \omega)]^{-1}, \quad (8)$$

and the full GW+DMFT self-energy defined as

$$\Sigma(\mathbf{k}, \omega) = \Sigma^{GW}(\mathbf{k}, \omega) + \Sigma_{\text{imp}}(\omega) - \Sigma_{\text{DC}}^{GW}(\omega). \quad (9)$$

Here,  $\mu$  is the chemical potential, which is adjusted during the DMFT self-consistency to ensure that the electron count of the impurity is correct.  $\mathbf{h}(\mathbf{k})$  is the bare one-particle Hamiltonian for the whole solid. We subtract the local  $G_0W_0$  self-energy in Eq. 9, and the DFT exchange-correlation potential is excluded from both the impurity and lattice self-energies, consequently our method exactly avoids double-counting. When the one-shot  $G_0W_0$  is used, it is not guaranteed that the GW+DMFT self-energy in Eq. 9 is strictly causal, and a fully self-consistent GW+DMFT is formally required [57]. However, in our test cases, we have not observed non-causal negative spectral functions at low-energies. Because multiple orbitals and atoms are

now chosen as the impurity, the final  $GW$ +DMFT self-energy does not strictly preserve all the symmetries of the solid, similar to other cellular DMFT methods [6]. Possible ways to alleviate this problem include incorporating more cells as the impurity, or deriving a translational and crystal symmetry invariant impurity Hamiltonian, as done in the dynamical cluster approximation (DCA) [7].

In order to use a wavefunction (Hamiltonian-)based impurity solver, we discretize  $\Delta(\omega)$ . We discretize along the real-frequency axis [58] so that dynamical quantities (e.g., spectral functions) are obtained more accurately. To obtain the discretization, we start with an initial guess by direct discretization on a numerical grid and optimize bath couplings  $\{V_{ip}^{(n)}\}$  and energies  $\{\epsilon_n\}$  to minimize a cost function over a range of real-frequency points (see Supplemental Material):

$$D = \sum_{\omega_l} \sum_{ij} \left( \Delta_{ij}(\omega_l + i\eta) - \sum_{n=1}^{N_\epsilon} \sum_{p=1}^{N_p} \frac{V_{ip}^{(n)} V_{jp}^{(n)}}{\omega_l + i\eta - \epsilon_n} \right)^2, \quad (10)$$

where  $N_\epsilon$  is the number of bath energies and  $N_p$  is the number of bath orbitals per bath energy, and we use a broadening factor  $\eta = 0.1$  a.u. unless specified. This optimization scheme is necessary to reduce the number of bath orbitals and avoid non-causal behavior in the  $GW$ +DMFT self-energies. The bath degrees of freedom are truncated by only coupling bath orbitals to the valence IAOs, further reducing computational and optimization costs. The full embedding problem with both impurity and bath orbitals is thus defined from the Hamiltonian

$$\hat{H}_{\text{emb}} = \hat{H}_{\text{imp}} + \sum_{n=1}^{N_\epsilon} \sum_{p=1}^{N_p} \left( \sum_i V_{ip}^{(n)} (a_i^\dagger a_{np} + a_{np}^\dagger a_i) + \epsilon_n a_{np}^\dagger a_{np} \right). \quad (11)$$

We solve for the ground-state and Green's functions of the impurity Hamiltonian using two quantum chemistry impurity solvers. For completeness, we give some general background on the solvers. The first is a CCSD Green's function solver at zero temperature. Our implementation of the CCSD Green's function solver is able to treat around 200 (impurity + bath) orbitals. At the singles and doubles level, CC may be viewed as generating ring, ladder, and coupled ring-ladder diagrams, and is exact for (arbitrary products of) two-electron problems regardless of interaction strength. CCSD is based on time-ordered diagrams, and the corresponding CCSD Green's function does not include contributions from all time-orderings of the ring diagrams that come from the  $GW$  self-energy, but contains a large number of vertex corrections to the self-energy and polarization propagator [59]. It has been shown to be accurate in a variety of settings, including simple metallic and ordered magnetic states in *ab initio* calculations [60–62], across weak to strong couplings when employed with small cluster DMFT impurities in Hubbard-like models [42], and in electron gases up to moderately dilute densities, e.g. that of metallic sodium [60]. Standard implementations of CCSD are capable of treating general Coulomb interactions and hybridizations, and recent work has demonstrated *ab initio* calculations in materials at finite temperatures [63, 64]. Similar to other

quantum chemistry based approaches, the efficiency of the CCSD method stems from taking advantage of the fact that many orbitals (e.g., far from the Fermi surface) are nearly full or empty. However, it is less suited to spin-fluctuations, and because CCSD truncates the coupled-cluster excitations at low order, it will break down when large spin fluctuations connecting many electrons simultaneously appear. In practice, a key indicator for the breakdown of CCSD is the magnitude of its excitation amplitudes, with large amplitudes suggesting inaccurate results.

In cases where CCSD breaks down, one can use higher excitation levels in CC [60], or other impurity solvers can be employed. Other interesting quantum chemistry solvers in this context include quantum chemistry DMRG (QC-DMRG) [65] and selected configuration interaction (selected CI) [41, 44, 66, 67] methods. For example, QC-DMRG offers a robust way to obtain correlated ground-states in complex systems [68] and *ab initio* Green's functions with up to 50 or more strongly correlated orbitals [69]. Selected CI methods are based on an excitation picture, and thus are very efficient with large numbers of nearly filled and empty orbitals ( $\sim 200$ ), although they are limited to smaller numbers of strongly correlated orbitals than DMRG ( $\sim 20$ ). These two solvers are systematically improvable towards numerical exactness, by decreasing the selection threshold (selected CI) or increasing the bond dimension (DMRG). To illustrate the generality of our embedding framework as well as to benchmark the accuracy of the CCSD solver, we show results also from a selected CI impurity solver (based on the semistochastic heat-bath configuration interaction (SHCI) method [44, 70–72]) within our  $GW$ +DMFT approach and apply it to the correlated metal  $\text{SrMoO}_3$ .

From the impurity Green's functions computed by the CCSD or SHCI solvers, we obtain an updated impurity self-energy  $\Sigma_{\text{imp}}(\omega)$ , and from this the DMFT cycle (Eqs. 7-11) is iterated until convergence between the impurity and lattice Green's functions:

$$\mathbf{G}_{\text{imp}}(\omega) = \mathbf{G}(\mathbf{R} = \mathbf{0}, \omega). \quad (12)$$

### III. RESULTS

We first apply our method to crystalline silicon. Although Si is considered a weakly-correlated semiconductor, it is still a challenging system for many DFT functionals (such as LDA and GGA) which do not yield accurate band gaps [73]. One-shot  $G_0W_0$  on top of LDA or GGA is known to significantly improve the band structure, although this relies somewhat on the cancellation of errors [74]. Such a small band-gap system also poses challenges to quantum embedding methods that start from a local correlation picture, such as DMFT [75], due to the long-range nature of its statically screened Coulomb interaction, which must be included in the treatment.

The full cell  $GW$ +DMFT results for Si are presented in Fig. 2. We used the GTH-PADE pseudopotentials [76] and GTH-TZVP basis [77], and a  $6 \times 6 \times 6$   $\Gamma$ -centered  $\mathbf{k}$ -point sampling. The impurity was defined as the unit cell of 2 Si atoms with 34 local orbitals ( $3s3p3d4s4p5s5p$  for Si), and



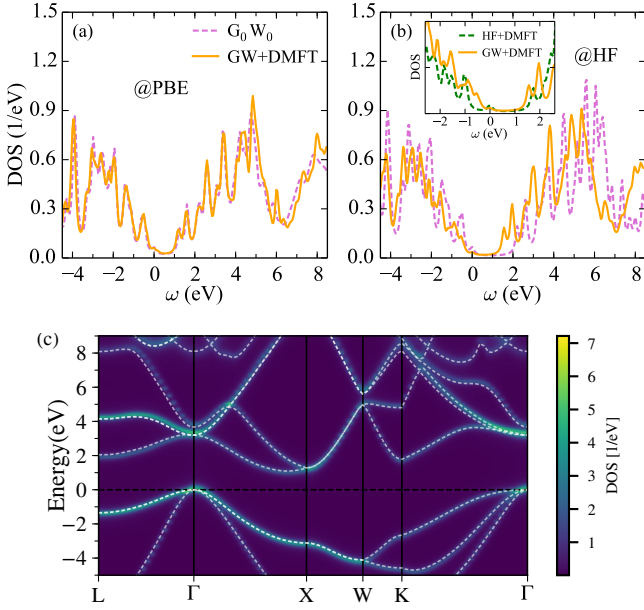


FIG. 2. Full cell  $G_0W_0$  results for silicon. (a)(b) Local spectral function from  $G_0W_0$  (PBE reference) and  $G_0W_0$  (HF reference). Inset of (b):  $G_0W_0$  compared to HF+DMFT ( $4 \times 4 \times 4$   $\mathbf{k}$ -mesh and GTH-DZVP basis) DOS taken from Ref. [39]. (c) Band structure starting from PBE orbitals. The heat map represents the  $G_0W_0$ @PBE result and the dashed line gives the  $G_0W_0$  bands. A broadening factor of 0.1 eV is used.

128 bath orbitals were used. As known from other  $G_0W_0$  calculations [78] and as seen in Figs. 2(a) and 2(b), the mean-field starting point strongly affects the quality of the  $G_0W_0$  results;  $G_0W_0$ @PBE gives an accurate band gap of 1.09 eV when compared to the experimental value of 1.17 eV [79], while  $G_0W_0$ @HF overestimates the band gap, giving 2.04 eV.  $G_0W_0$ DMFT predicts the band gap of Si to be 1.01 eV (@PBE) and 1.39 eV (@HF), largely removing the reference dependence of  $G_0W_0$ , due to the more complete inclusion of diagrams from interactions within the unit cell. The spectral function is also greatly improved in  $G_0W_0$ DMFT compared to  $G_0W_0$ @HF. In earlier HF+DMFT calculations [39] (see inset of Fig. 2(b)), we found the band gap to be too large by 0.5 eV, and this quantifies the effect of the long-range correlations in  $G_0W_0$  on the band gap of Si. From Fig. 2(c), we note that  $G_0W_0$ DMFT@PBE maintains the accurate band structure of  $G_0W_0$ @PBE, in contrast to self-consistent GW, which is known to lead to worse results than  $G_0W_0$  itself [80, 81].

We next show the results of full cell  $G_0W_0$ DMFT in Fig. 3 for a strongly-correlated insulator, NiO, in the antiferromagnetic phase. The GTH-PADE pseudopotential and GTH-DZVP-MOLOPT-SR basis set [83] were used with a  $6 \times 6 \times 6$   $\Gamma$ -centered  $\mathbf{k}$ -point sampling defined with respect to the antiferromagnetic cell (2 NiO units). (As an estimate of the remaining finite size error, the difference between the  $G_0W_0$ @PBE gaps for  $4 \times 4 \times 4$  and  $6 \times 6 \times 6$   $\mathbf{k}$ -meshes is only 0.1 eV). We used the antiferromagnetic cell of 2 NiO units along the [111] direction as the impurity, corresponding to 78 impurity orbitals ( $3s3p3d4s4p4d4f5s$  for Ni and  $2s2p3s3p3d$

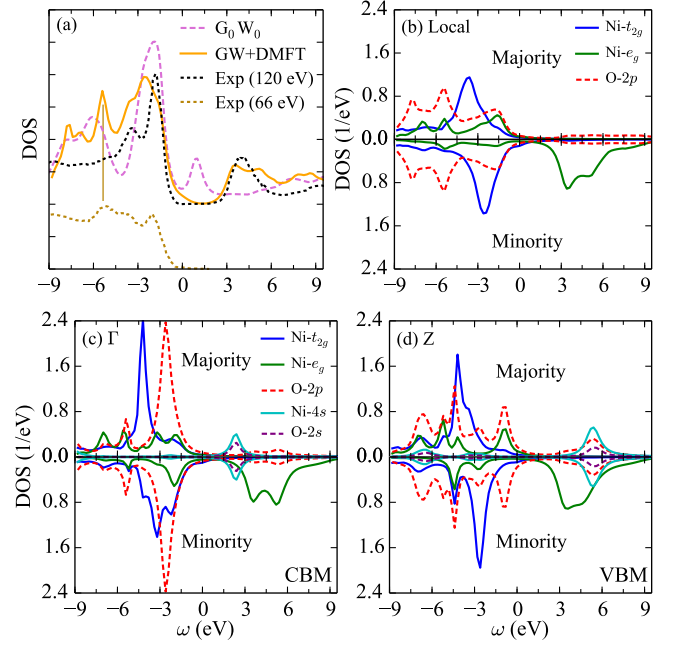


FIG. 3. Full cell  $G_0W_0$ DMFT results for NiO (AFM phase) based on the PBE reference. (a) Local DOS. The experimental spectra are taken from Ref. [82]. (b) Orbital-resolved local DOS. (c)(d) Orbital-resolved and momentum-resolved DOS at the  $\Gamma$  point (CBM) and  $Z = (0.5, 0.5, 0.5)$  point (VBM). A broadening factor of 0.4 eV is used.

for O) and 72 bath orbitals in the DMFT impurity problem. As seen in Fig. 3(a),  $G_0W_0$ @PBE severely underestimates the band gap at 1.9 eV, even when using a spin symmetry broken PBE reference. We note that the quality of GW in this material is strongly dependent on the initial choice of Hamiltonian, and in practice improves through self-consistency, as has been seen in self-consistent quasiparticle GW calculations [84]. Meanwhile, the valence spectrum of  $G_0W_0$ @PBE does not agree well with the experimental photoemission spectrum measured at a photon energy of 120 eV [82]. We note that the experimental spectra do not report photoemission intensity in absolute units, so we rescale the spectra to make the main valence peaks of the experimental and  $G_0W_0$ DMFT spectra approximately the same height, to facilitate comparison.  $G_0W_0$ DMFT, on the other hand, predicts a band gap of 4.0 eV and a magnetic moment of  $1.69 \mu_B$ , both in very good agreement with the experimental values of 4.3 eV [82] and  $1.77$ - $1.90 \mu_B$  [85, 86]. More interestingly, our  $G_0W_0$ DMFT DOS captures the experimental two-peak structure of the valence spectrum around  $-2$  and  $-3$  eV. A detailed analysis of the spin-orbital-resolved local DOS in Fig. 3(b) reveals that this two-peak structure results from the splitting of the majority and minority spin components of the  $\text{Ni-}t_{2g}$  orbitals, and is a signature of the AFM phase, as it does not arise within the paramagnetic phase [87]. Compared to the experimental valence spectrum measured at a lower photon energy (66 eV) that mainly probes O-2p states, we find that our  $G_0W_0$ DMFT DOS agrees very well with the experimental peak at  $-5$  eV, suggesting we have achieved a quantitative description of both local and non-local states in NiO. Our

GW+DMFT method also predicts a satellite peak around -8 eV, consistent with the photoemission spectrum in Ref. [88]. We find this valence peak has a significant contribution from O-2p orbitals, and a less substantial Ni-3d weight. From the local DOS, we can also conclude that NiO is an insulator with mixed charge-transfer and Mott character, with a valence band with contributions from Ni- $t_{2g}$ , Ni- $e_g$  and O-2p, and a conduction band that is mainly of Ni- $e_g$  character.

In Figs. 3(c) and 3(d), we further analyze the character of the conduction band minimum (CBM) and valence band maximum (VBM) in the Brillouin zone using the momentum-resolved DOS. We find that the lowest conduction band has strong Ni-4s and O-2s character at the  $\Gamma$  point (CBM), which was not discussed in many earlier DMFT calculations [28, 89, 90] which focused on the Ni-3d and O-2p orbitals and thus did not include Ni-4s (or O-2s) orbitals in the impurity (although see Ref. [91] for a notable exception), unlike our full cell GW+DMFT treatment. At the Z point (VBM), we find that the highest valence band has significant O-2p and Ni- $e_g$  contributions, with very little Ni- $t_{2g}$  character. This is very different from the local DOS, where the Ni- $t_{2g}$  has dominant weight in the valence bands. We confirm this by plotting the spatially-resolved DOS of NiO in the (001) plane in Fig. 4. We see that at the first valence peak and around the Ni atoms, the local spatial DOS has a Ni- $t_{2g}$  ( $d_{xy}$ ) orbital shape, while the momentum-resolved spatial DOS (at the Z point) has a Ni- $e_g$  ( $d_{x^2-y^2}$ ) orbital shape. Further, the weight of the DOS around the O atoms in Fig. 4(b) is considerably larger than in Fig. 4(a).

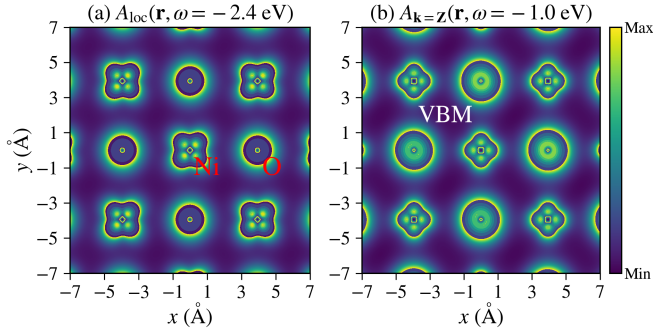


FIG. 4. Spatially-resolved DOS from GW+DMFT (PBE reference) for NiO in the (001) plane. (a) Local DOS at  $\omega = -2.4$  eV. (b) Momentum-resolved DOS at VBM energy  $\omega = -1.0$  eV and Z = (0.5, 0.5, 0.5) point.

Since our impurity includes two NiO units, we can also look at correlations across the cells. We computed the spin-spin correlation function for the Ni atoms within the impurity problem:

$$\sum_{i \in \text{Ni}_1, j \in \text{Ni}_2} \langle \mathbf{S}_i \cdot \mathbf{S}_j \rangle = \sum_{i \in \text{Ni}_1, j \in \text{Ni}_2} \sum_{a=x,y,z} \langle S_i^a S_j^a \rangle. \quad (13)$$

We found  $\langle \mathbf{S}_i \cdot \mathbf{S}_j \rangle$  between two Ni atoms to be -0.707. Both  $\langle S_i^x S_j^x \rangle$  and  $\langle S_i^y S_j^y \rangle$  contribute almost zero spin correlation, and the uncorrelated value  $\langle S_i^z \rangle \langle S_j^z \rangle$  is -0.710, suggesting that quantum spin correlations are weak and NiO is close to a classical Ising magnet. This is consistent with experimental mea-

surements of the critical behavior of the magnetic phase transition in NiO [92] and our previous *ab initio* DMET study [38].

We next turn to study a second strongly-correlated insulator, hematite ( $\alpha$ -Fe<sub>2</sub>O<sub>3</sub>), in the AFM phase. We take the impurity to be the complete AFM unit cell, including 2 Fe<sub>2</sub>O<sub>3</sub> units (Fig. 1), with a “+ - + -” type AFM ordering of the Fe spins. Because of the large impurity size, we used a DZV-quality basis (GTH-DZV-MOLOPT-SR, 3s3p3d4s4p4d5s for Fe, 2s2p3s3p for O), leading to an impurity problem with 124 impurity and 48 bath orbitals. The small number of bath orbitals is due to the current numerical limitations of our CCSD solver. However, since our bath orbitals are only coupled to the valence impurity orbitals, and we aim to reproduce the hybridization only in a window near the Fermi level ( $\pm 0.4$  a.u.), the bath discretization error is not too severe. Numerical tests (Supplemental Material) suggest that the finite bath discretization introduces an error of 0.05  $\mu_B$  in the Fe magnetic moment, while the band gap uncertainty is within 0.4 eV. The 3s3p orbitals of Fe were treated as frozen core orbitals (i.e., uncorrelated) in the CCSD solver. The GTH-PBE pseudopotential and  $4 \times 4 \times 4$   $\Gamma$ -centered  $\mathbf{k}$ -point sampling were employed. As presented in Fig. 5(a),  $G_0W_0$ @PBE severely underestimates the band gap at 0.5 eV, compared to the experimental value of 2.6 eV [93].  $G_0W_0$  with the hybrid functional PBE0 slightly overestimates the gap (3.4 eV), but the spectrum does not agree well with experiment, and in particular, the features of the  $G_0W_0$ @PBE0 DOS are too sharp around -7 and 3.5 eV (Fig. 5(b)).

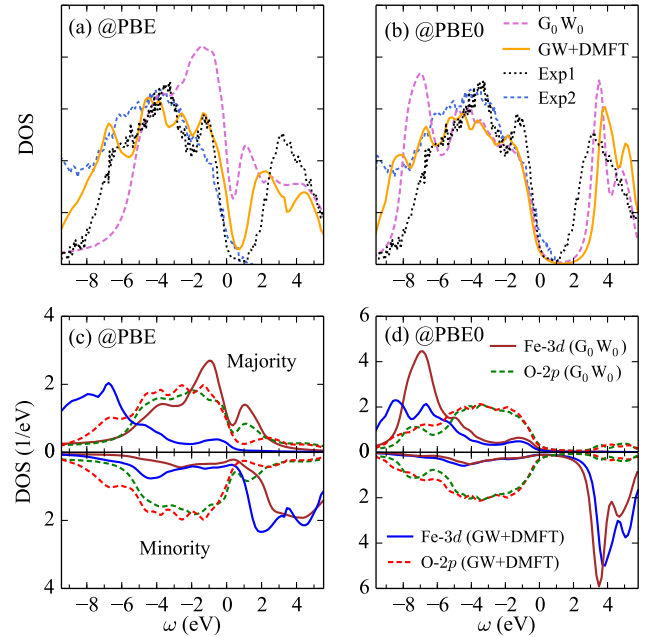


FIG. 5. Full cell GW+DMFT results for  $\alpha$ -Fe<sub>2</sub>O<sub>3</sub> (AFM phase). (a)(b) Local DOS based on PBE and PBE0 references. The experimental spectra are taken from Ref. [93] (exp1) and Ref. [94] (exp2). (c)(d) Orbital-resolved DOS corresponding to (a)(b). A broadening factor of 0.3 eV is used.

GW+DMFT improves the  $G_0W_0$ @PBE spectrum signifi-

cantly, especially in the valence region, although the band gap (1.5 eV) is still too small. From the orbital-resolved DOS in Fig. 5(c), we find that the main improvement comes from the spectral positions of the majority spin component of the Fe-3d orbitals and O-2p orbitals.  $G_0W_0$ @PBE mistakenly predicts the Fe-3d valence spectrum to lie close to the Fermi level and that  $\text{Fe}_2\text{O}_3$  has considerable Mott insulating character. However,  $\text{GW}+\text{DMFT}$  shifts the majority-spin Fe-3d DOS to lower energies, consistent with previous DFT+DMFT calculations [95, 96]. Because of this correction,  $\text{GW}+\text{DMFT}$  obtains a more accurate Fe magnetic moment than PBE ( $4.23 \mu_B$  compared to  $3.71 \mu_B$  with the experimental moment being  $4.64 \mu_B$  [97]). While the  $\text{GW}+\text{DMFT}$  DOS does not agree well with the “exp1” spectrum [93] below -7 eV, we observe a much better agreement between  $\text{GW}+\text{DMFT}$  and the “exp2” spectrum [94], likely due to different experimental settings. We find that the valence band spectrum is dominated by O-2p near the Fermi level, indicating that  $\text{Fe}_2\text{O}_3$  is in fact a pure charge-transfer insulator, with almost no Mott insulating character. This is in contrast to DFT+DMFT calculations [95, 96] that find a sizable Fe-3d contribution to the valence band maximum. We attribute this disagreement to the full cell  $\text{GW}+\text{DMFT}$  treatment where both O-2p orbitals and Fe-3d are treated on an equal footing at the impurity level, which thus allows for a more accurate balancing of their relative contributions to the spectral weight.

Starting from a PBE0 reference,  $\text{GW}+\text{DMFT}$  finds a slightly larger band gap (3.9 eV) and magnetic moment ( $4.37 \mu_B$ ) than  $G_0W_0$  (3.4 eV and  $4.20 \mu_B$ ). The overly sharp peaks of the  $G_0W_0$ @PBE0 spectrum around -7 and 3.5 eV are corrected by  $\text{GW}+\text{DMFT}$ , which broadens the Fe-3d peaks as shown in Fig. 5(d). Comparing results between the PBE and PBE0 references, the severe reference dependence of spectral functions (especially Fe-3d states) is largely reduced by  $\text{GW}+\text{DMFT}$ . In summary, it appears we achieve a good description of the photoemission spectrum for  $\text{Fe}_2\text{O}_3$  within the full cell  $\text{GW}+\text{DMFT}$ , although a fully quantitative prediction of the band gap is not attained. Given that  $G_0W_0$  only provides a minor correction to the underlying DFT band gap in this system, the likely culprit is the insufficiency of the  $G_0W_0$  approximation in describing the long-range interactions in  $\text{Fe}_2\text{O}_3$ .

We finally investigate a perovskite-type paramagnetic correlated metal  $\text{SrMoO}_3$  with two electrons ( $4d^2$ ) occupying the Mo- $t_{2g}$  bands. We simulated the cubic structure of  $\text{SrMoO}_3$  using the GTH-PADE pseudopotential and GTH-DZVP-MOLOPT-SR basis set, with a  $\Gamma$ -centered  $6 \times 6 \times 6$   $\mathbf{k}$ -mesh. To facilitate comparison with previous numerical studies, we used LDA as the underlying DFT functional. The  $\text{SrMoO}_3$  unit cell was taken as the DMFT impurity, corresponding to 71 impurity orbitals ( $4d4f5s5p5d6s$  for Mo,  $2s2p3s3p3d$  for O,  $4d5s5p6s$  for Sr) and 117 bath orbitals. For paramagnetic metals, the quasiparticle peaks are expected to be sharp near the Fermi level, so we used a much smaller broadening ( $\eta = 0.02$  a.u.) when discretizing the hybridization on the real axis. We found this small broadening is crucial for avoiding non-causal behavior in the computed self-energies.

As the electronic structure of  $\text{SrMoO}_3$  near the Fermi level

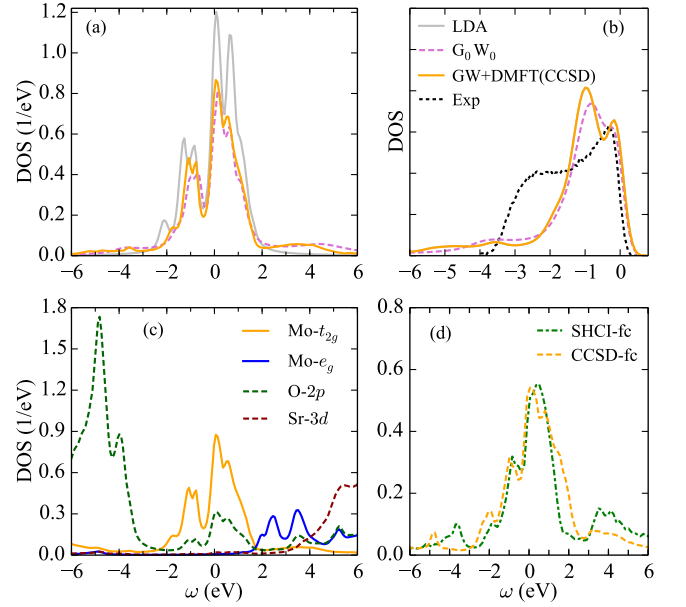


FIG. 6. Full cell  $\text{GW}+\text{DMFT}$  results for paramagnetic  $\text{SrMoO}_3$  based on the LDA reference. (a) Local DOS of Mo- $t_{2g}$  bands computed with a broadening of 0.15 eV. (b) Comparison of  $G_0W_0$  and  $\text{GW}+\text{DMFT}$  with photoemission experimental data [98]. A Fermi function of 298 K and a Gaussian filter of 0.2 eV are applied to the calculated DOS to match the experimental resolution. (c) Orbital-resolved DOS computed by  $\text{GW}+\text{DMFT}$  (CCSD). (d) Comparison of  $\text{GW}+\text{DMFT}$  DOS (Mo- $t_{2g}$  bands) using CCSD and SHCI solvers in a frozen-core correlated space.

is dominated by Mo- $t_{2g}$  bands, we mainly discuss spectral functions of Mo- $t_{2g}$  bands in Fig. 6, although the orbital-resolved DOS is also included in Fig. 6(c). As shown in Fig. 6(a),  $G_0W_0$ @LDA shows a small band narrowing compared to LDA, where the bandwidth is reduced from 3.9 eV (LDA) to 3.2 eV ( $G_0W_0$ ).  $\text{GW}+\text{DMFT}$  with the CCSD solver predicts a slightly larger bandwidth of 3.5 eV than  $G_0W_0$  and similar quasiparticle bands near the Fermi level, which are clearly renormalized compared to LDA. In Ref. [98], an obvious narrowing of the quasiparticle bands compared to the LDA band structure calculation was not observed in the photoemission spectrum, which is incompatible with the measured enhancement of specific heat. This phenomenon was attributed to Hund’s rule coupling, which induces strong quasiparticle renormalization even when the Hubbard interaction values are smaller than the overall bandwidth. Our  $G_0W_0$  and  $\text{GW}+\text{DMFT}$  results are consistent with this observation.

We further found a lower and upper sideband in the  $G_0W_0$ @LDA spectrum, located around -3 and 4.5 eV.  $\text{GW}+\text{DMFT}$  gives similar sidebands as  $G_0W_0$ , but the position of the upper sideband is shifted to a lower value of 3.5 eV. As shown in Fig. 6(b), the experimental photoemission spectrum shows a substantial hump around -2.5 eV, which was not captured by the LDA+DMFT calculations. The authors in Ref. [98] thus concluded this hump is likely a plasmon satellite, and proper treatment of long-range correlations is required to capture this effect. To compare with the pho-



to emission spectrum, we applied a Fermi function of 298 K and a Gaussian filter of 0.2 eV on our calculated spectral functions to match the experimental resolution. We found that the quasiparticle bands near the Fermi level agree well with experiment in both  $G_0W_0$  and  $GW+DMFT$ . However, although our  $G_0W_0$  and  $GW+DMFT$  results predict sizable sidebands around -3 eV, the relative spectral weight of the sideband is too weak compared to experiment. This experimental hump is also unlikely to originate from other states in  $\text{SrMoO}_3$ , as the  $GW+DMFT$  O-2*p* spectrum intensity is weak in the region of -3 to -2 eV as seen in Fig. 6(c). On one hand, this could indicate that larger impurity cells may be necessary in the full cell  $GW+DMFT$  approach to properly capture the strong plasmon intensity. However, we note that our results are in agreement with other  $GW+DMFT$  calculations [24, 30], which may also suggest that the satellite intensity is overestimated in the experiment due to insufficiently high photon energies, or oxygen defects.

To demonstrate the use of a different quantum chemistry solver, and to benchmark the accuracy of our CCSD results for  $\text{SrMoO}_3$  we also carried out calculations using the SHCI solver [44, 70, 71], within the full cell  $GW+DMFT$ , as shown in Fig. 6(d). Because SHCI is much more computationally demanding than CCSD, we only performed a one-shot SHCI calculation on the impurity problem derived from the self-consistent  $GW+DMFT$  solution using the CCSD solver, and used a variational threshold of  $\epsilon = 6 \times 10^{-4}$  Hartrees to select determinants. A modified version of the Arrow code [72] was then used to compute the SHCI Green's function. To allow for a fair comparison, we restricted the number of correlated electrons and orbitals in SHCI and CCSD to be identical (30 electrons in 131 orbitals), obtained by freezing the lowest 57 occupied orbitals in the HF solution of the impurity problem. Comparing the resulting  $GW+DMFT$  Mo-*t*<sub>2g</sub> DOS, we find that the CCSD and SHCI spectrum agrees very well in  $\text{SrMoO}_3$ , although SHCI predicts a slightly smaller bandwidth and stronger sideband intensity than CCSD.

Lastly, in Fig. 7, we perform an analysis to understand the role of intermediate range interactions and vertex corrections that are now captured within our full cell  $GW+DMFT$  method but omitted in the usual downfolding based  $GW+DMFT$  treatments. In the systems studied here, one way in which this shows up is in quantitative corrections to the physics of the non-*d* orbitals of metal and non-metal atoms, which are normally only treated at the DFT or  $GW$  level. As shown in Fig. 7(a) and (c), there are significant vertex corrections to the self-energies of the O-2*p* and Ni-4*s* orbitals in NiO and O-2*p* orbitals in  $\text{SrMoO}_3$  when using the full cell  $GW+DMFT$  method. Such vertex corrections lead to non-trivial effects on the spectral functions of the non-*d* orbitals. For example, the peak position and intensity of O-2*p* DOS is clearly changed in both NiO and  $\text{SrMoO}_3$ , when comparing the full and local (i.e., only Ni-3*d* or Mo-4*d*) self-energy corrections ( $\Sigma^{\text{CC}} - \Sigma^{\text{GW}}$ ). Furthermore, because some non-*d* orbitals are strongly hybridized with the *d* orbitals, correcting the non-*d* orbitals also modifies the *d*-orbital DOS in NiO and  $\text{SrMoO}_3$ . Meanwhile, in Fig. 7(e), we show that vertex corrections to the self-energies across two Si atoms within the impurity cell

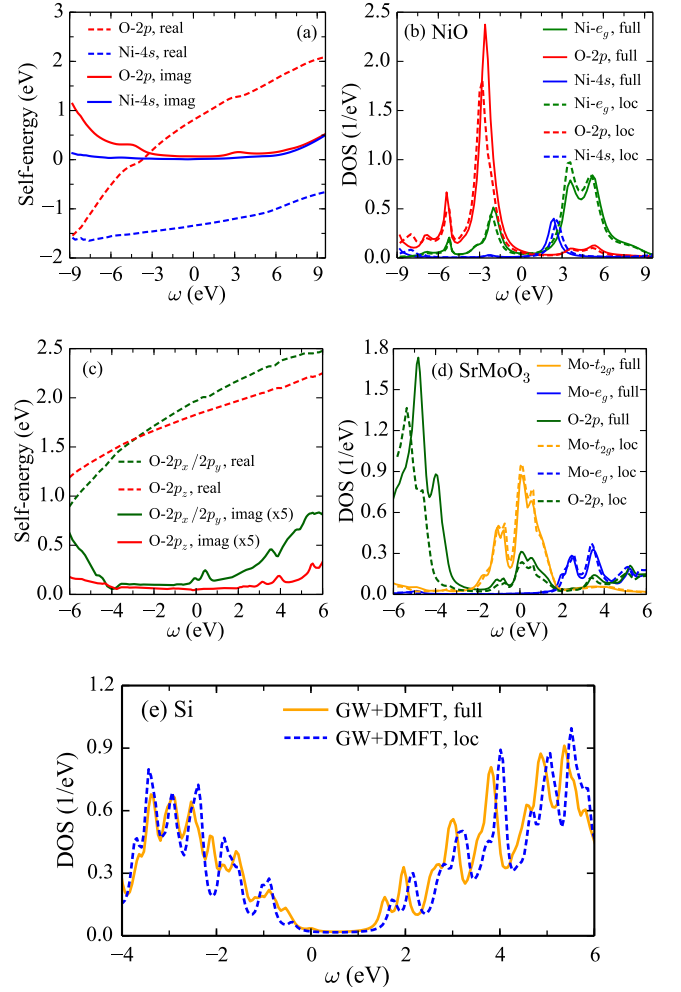


FIG. 7. Effects of non-*d*-orbital vertex corrections to the self-energy ( $\Sigma^{\text{CC}} - \Sigma^{\text{GW}}$ ) on the full cell  $GW+DMFT$  results. (a) DMFT self-energy corrections to the O-2*p* and Ni-4*s* orbitals in NiO. (b)  $GW+DMFT$   $\mathbf{k}$ -resolved DOS of NiO at the  $\Gamma$  point, obtained by adding the self-energy correction to all impurity orbitals (“full”) or only the Ni-3*d* orbitals (“loc”). (c) DMFT self-energy corrections to O-2*p* orbitals in  $\text{SrMoO}_3$ . (d)  $GW+DMFT$  local DOS of  $\text{SrMoO}_3$ , obtained by adding the self-energy correction to all impurity orbitals (“full”) or only the Mo-4*d* orbitals (“loc”). (e)  $GW+DMFT$  local DOS of Si (HF reference), obtained by adding the self-energy correction to all impurity orbitals (“full”) or only the 3*s*3*p* orbitals within each Si atom (“loc”).

also lead to quantitative changes in the  $GW+DMFT$  DOS of Si (based on the HF reference). In summary, our full cell  $GW+DMFT$  provides vertex corrections to all orbitals, which is known to be necessary to achieve quantitative accuracy in many kinds of *ab initio* simulations [24].

#### IV. CONCLUSIONS

In this work, we introduced a full cell  $GW+DMFT$  formulation for the *ab initio* simulation of correlated materials. The primary strength of this approach is that it entirely avoids the



problem of selecting a low-energy subspace, and consequently the uncontrolled errors introduced either by downfolding the effective interactions within the subspace, or via DFT double counting. The resulting method is then fully diagrammatically controlled and can easily treat all interactions, and provides a framework to apply advanced quantum chemistry methods to study correlated solids. We showed that full cell  $GW+DMFT$  can be applied to systems using impurity cells of up to 10 atoms in calculations of the spectral properties of Si, NiO,  $\alpha$ - $Fe_2O_3$  and  $SrMoO_3$ , obtaining for most quantities, results of good quantitative accuracy. By defining the impurity to comprise all orbitals in the AFM supercells of NiO and  $\alpha$ - $Fe_2O_3$ , we also showed how the full cell approach can cleanly differentiate between different amounts of charge-transfer and Mott insulating character and the orbital character around the gap, as both metal and non-metal orbitals enter into the impurity prob-

lem on an equal footing. Overall, our calculations demonstrate the potential of the full cell  $GW+DMFT$  approach for studies of more complicated materials, en route towards a fully predictive theory of correlated materials.

## ACKNOWLEDGMENTS

This work was supported by the US Department of Energy via the M<sup>2</sup>QM EFRC under award no. de-sc0019330. We thank Cyrus Umrigar and Yuan Yao for providing the SHCI Green's function code. TZ thank helpful discussions from Zhihao Cui, Xing Zhang and Timothy Berkelbach. Additional support was provided by the Simons Foundation via the Simons Collaboration on the Many Electron Problem, and via the Simons Investigatorship in Physics.

- 
- [1] P. R. Kent and G. Kotliar, *Science* **361**, 348 (2018).
  - [2] A. Georges and G. Kotliar, *Phys. Rev. B* **45**, 6479 (1992).
  - [3] A. Georges, G. Kotliar, W. Krauth, and M. Rozenberg, *Rev. Mod. Phys.* **68**, 13 (1996).
  - [4] G. Knizia and G. K.-L. Chan, *Phys. Rev. Lett.* **109**, 186404 (2012).
  - [5] Q. Sun and G. K.-L. Chan, *Acc. Chem. Res.* **49**, 2705 (2016), [arXiv:1612.02576](#).
  - [6] G. Kotliar, S. Y. Savrasov, G. Pálsson, and G. Biroli, *Phys. Rev. Lett.* **87**, 186401 (2001), [arXiv:0010328 \[cond-mat\]](#).
  - [7] M. Hettler, M. Mukherjee, M. Jarrell, and H. Krishnamurthy, *Phys. Rev. B* **61**, 12739 (2000).
  - [8] W. Kohn and L. J. Sham, *Phys. Rev.* **140**, A1133 (1965).
  - [9] K. Held, I. A. Nekrasov, G. Keller, V. Eyert, N. Blümer, A. K. McMahan, R. T. Scalettar, T. Pruschke, V. I. Anisimov, and D. Vollhardt, *Phys. status solidi* **243**, 2599 (2006).
  - [10] G. Kotliar, S. Y. Savrasov, K. Haule, V. S. Oudovenko, O. Parcollet, and C. A. Marianetti, *Rev. Mod. Phys.* **78**, 865 (2006).
  - [11] K. Held, *Adv. Phys.* **56**, 829 (2007).
  - [12] F. Nilsson and F. Aryasetiawan, *Computation* **6**, 26 (2018).
  - [13] F. Aryasetiawan, M. Imada, A. Georges, G. Kotliar, S. Biermann, and A. I. Lichtenstein, *Phys. Rev. B* **70**, 195104 (2004).
  - [14] X. Wang, M. J. Han, L. de' Medici, H. Park, C. A. Marianetti, and A. J. Millis, *Phys. Rev. B* **86**, 195136 (2012).
  - [15] K. Haule, *Phys. Rev. Lett.* **115**, 196403 (2015).
  - [16] M. Karolak, G. Ulm, T. Wehling, V. Mazurenko, A. Poteryaev, and A. Lichtenstein, *J. Electron Spectros. Relat. Phenom.* **181**, 11 (2010).
  - [17] J. P. Perdew, W. Yang, K. Burke, Z. Yang, E. K. Gross, M. Scheffler, G. E. Scuseria, T. M. Henderson, I. Y. Zhang, A. Ruzsinszky, H. Peng, J. Sun, E. Trushin, and A. Görling, *Proc. Natl. Acad. Sci. U. S. A.* **114**, 2801 (2017).
  - [18] L. Hedin, *Phys. Rev.* **139**, A796 (1965).
  - [19] M. S. Hybertsen and S. G. Louie, *Phys. Rev. B* **34**, 5390 (1986).
  - [20] M. Shishkin and G. Kresse, *Phys. Rev. B* **74**, 035101 (2006).
  - [21] P. Sun and G. Kotliar, *Phys. Rev. B* **66**, 085120 (2002).
  - [22] S. Biermann, F. Aryasetiawan, and A. Georges, *Phys. Rev. Lett.* **90**, 086402 (2003).
  - [23] L. Boehnke, F. Nilsson, F. Aryasetiawan, and P. Werner, *Phys. Rev. B* **94**, 201106 (2016).
  - [24] F. Nilsson, L. Boehnke, P. Werner, and F. Aryasetiawan, *Phys. Rev. Mater.* **1**, 043803 (2017), [arXiv:1706.06808](#).
  - [25] J. M. Tomczak, M. Casula, T. Miyake, F. Aryasetiawan, and S. Biermann, *EPL* **100**, 67001 (2012), [arXiv:1210.6580](#).
  - [26] C. Taranto, M. Kaltak, N. Parragh, G. Sangiovanni, G. Kresse, A. Toschi, and K. Held, *Phys. Rev. B* **88**, 165119 (2013), [arXiv:1211.1324](#).
  - [27] J. Tomczak, P. Liu, A. Toschi, G. Kresse, and K. Held, *Eur. Phys. J. Spec. Top.* **226**, 2565 (2017).
  - [28] S. Choi, A. Kutepov, K. Haule, M. van Schilfgaarde, and G. Kotliar, *npj Quantum Mater.* **1**, 16001 (2016).
  - [29] S. Choi, P. Semon, B. Kang, A. Kutepov, and G. Kotliar, *Comput. Phys. Commun.* **244**, 277 (2019), [arXiv:1810.01679](#).
  - [30] F. Petocchi, F. Nilsson, F. Aryasetiawan, and P. Werner, *Phys. Rev. Res.* **2**, 13191 (2020).
  - [31] T. N. Lan, A. Shee, J. Li, E. Gull, and D. Zgid, *Phys. Rev. B* **96**, 155106 (2017).
  - [32] S. Isakov, C.-N. Yeh, E. Gull, and D. Zgid, *Phys. Rev. B* **102**, 085105 (2020).
  - [33] D. H. Lu, M. Yi, S. K. Mo, A. S. Erickson, J. Analytis, J. H. Chu, D. J. Singh, Z. Hussain, T. H. Geballe, I. R. Fisher, and Z. X. Shen, *Nature* **455**, 81 (2008).
  - [34] C. Weber, K. Haule, and G. Kotliar, *Nat. Phys.* **6**, 574 (2010), [arXiv:1005.3095](#).
  - [35] B. Amadon, F. Lechermann, A. Georges, F. Jollet, T. O. Wehling, and A. I. Lichtenstein, *Phys. Rev. B* **77**, 205112 (2008).
  - [36] W. Chibani, X. Ren, M. Scheffler, and P. Rinke, *Phys. Rev. B* **93**, 165106 (2016), [arXiv:1506.03680](#).
  - [37] Q. Sun, T. C. Berkelbach, N. S. Blunt, G. H. Booth, S. Guo, Z. Li, J. Liu, J. D. McClain, E. R. Sayfutyarova, S. Sharma, S. Wouters, and G. K.-L. Chan, *Wiley Interdiscip. Rev. Comput. Mol. Sci.* **8**, e1340 (2018).
  - [38] Z. H. Cui, T. Zhu, and G. K.-L. Chan, *J. Chem. Theory Comput.* **16**, 119 (2020), [arXiv:1909.08596](#).
  - [39] T. Zhu, Z.-H. Cui, and G. K.-L. Chan, *J. Chem. Theory Comput.* **16**, 141 (2020).
  - [40] D. Zgid and G. K.-L. Chan, *J. Chem. Phys.* **134**, 094115 (2011).
  - [41] D. Zgid, E. Gull, and G. K. L. Chan, *Phys. Rev. B* **86**, 1 (2012), [arXiv:1203.1914](#).
  - [42] T. Zhu, C. A. Jiménez-Hoyos, J. McClain, T. C. Berkelbach, and G. K.-L. Chan, *Phys. Rev. B* **100**, 115154 (2019).
  - [43] A. Shee and D. Zgid, *J. Chem. Theory Comput.* **15**, 6010 (2019).

- [44] A. A. Holmes, N. M. Tubman, and C. J. Umrigar, *J. Chem. Theory Comput.* **12**, 3674 (2016).
- [45] Y. Lu, M. Höppner, O. Gunnarsson, and M. Haverkort, *Phys. Rev. B* **90**, 085102 (2014).
- [46] A. Go and A. J. Millis, *Phys. Rev. B* **96**, 1 (2017), [arXiv:1703.04928](#).
- [47] Q. Sun, T. C. Berkelbach, J. D. McClain, and G. K.-L. Chan, *J. Chem. Phys.* **147**, 164119 (2017).
- [48] X. Ren, P. Rinke, V. Blum, J. Wieferink, A. Tkatchenko, A. Sanfilippo, K. Reuter, and M. Scheffler, *New J. Phys.* **14**, 053020 (2012), [arXiv:1201.0655](#).
- [49] J. Wilhelm, M. Del Ben, and J. Hutter, *J. Chem. Theory Comput.* **12**, 3623 (2016).
- [50] G. H. Booth, T. Tsatsoulis, G. K. L. Chan, and A. Grüneis, *J. Chem. Phys.* **145**, 084111 (2016), [arXiv:1603.06457](#).
- [51] H. J. Vidberg and J. W. Serene, *J. Low Temp. Phys.* **29**, 179 (1977).
- [52] T. Zhu and G. K.-L. Chan, [arXiv: 2007.03148](#) (2020), [arXiv:2007.03148](#).
- [53] R. W. Godby, M. Schlüter, and L. J. Sham, *Phys. Rev. B* **37**, 10159 (1988).
- [54] G. Knizia, *J. Chem. Theory Comput.* **9**, 4834 (2013).
- [55] P. Liu, M. Kaltak, J. Klimeš, and G. Kresse, *Phys. Rev. B* **94**, 165109 (2016), [arXiv:1607.02859](#).
- [56] J. Wilhelm, D. Golze, L. Talirz, J. Hutter, and C. A. Pignedoli, *J. Phys. Chem. Lett.* **9**, 306 (2018).
- [57] J. Lee and K. Haule, *Phys. Rev. B* **95**, 155104 (2017), [arXiv:1611.07090](#).
- [58] I. de Vega, U. Schollwöck, and F. A. Wolf, *Phys. Rev. B* **92**, 155126 (2015).
- [59] M. F. Lange and T. C. Berkelbach, *J. Chem. Theory Comput.* **14**, 4224 (2018), [arXiv:1805.00043](#).
- [60] J. McClain, J. Lischner, T. Watson, D. A. Matthews, E. Ronca, S. G. Louie, T. C. Berkelbach, and G. K.-L. Chan, *Phys. Rev. B* **93**, 235139 (2016).
- [61] Y. Gao, Q. Sun, J. M. Yu, M. Motta, J. McClain, A. F. White, A. J. Minnich, and G. K. L. Chan, *Phys. Rev. B* **101**, 165138 (2020), [arXiv:1910.02191](#).
- [62] K. T. Williams, Y. Yao, J. Li, L. Chen, H. Shi, M. Motta, C. Niu, U. Ray, S. Guo, R. J. Anderson, J. Li, L. N. Tran, C.-N. Yeh, B. Mussard, S. Sharma, F. Bruneval, M. van Schilfgaarde, G. H. Booth, G. K.-L. Chan, S. Zhang, E. Gull, D. Zgid, A. Millis, C. J. Umrigar, and L. K. Wagner, *Phys. Rev. X* **10**, 011041 (2020).
- [63] A. F. White and G. K.-L. Chan, *J. Chem. Theory Comput.* **14**, 5690 (2018).
- [64] A. F. White and G. Kin-Lic Chan, *J. Chem. Phys.* **152**, 224104 (2020), [arXiv:2004.01729](#).
- [65] G. K.-L. Chan and S. Sharma, *Annu. Rev. Phys. Chem.* **62**, 465 (2011).
- [66] B. Huron, J. P. Malrieu, and P. Rancurel, *J. Chem. Phys.* **58**, 5745 (1973).
- [67] C. Mejuto-Zaera, N. M. Tubman, and K. B. Whaley, *Phys. Rev. B* **100**, 125165 (2019).
- [68] Z. Li, S. Guo, Q. Sun, and G. K.-L. Chan, *Nat. Chem.* **11**, 1026 (2019).
- [69] E. Ronca, Z. Li, C. A. Jimenez-Hoyos, and G. K.-L. Chan, *J. Chem. Theory Comput.* **13**, 5560 (2017), [arXiv:1706.09537](#).
- [70] S. Sharma, A. A. Holmes, G. Jeanmairet, A. Alavi, and C. J. Umrigar, *J. Chem. Theory Comput.* **13**, 1595 (2017), [arXiv:1610.06660](#).
- [71] J. Li, M. Otten, A. A. Holmes, S. Sharma, and C. J. Umrigar, *J. Chem. Phys.* **149**, 214110 (2018), [arXiv:1809.04600](#).
- [72] Y. Yao, C. J. Umrigar, T. Zhu, and G. K.-L. Chan, Unpublished.
- [73] J. Heyd, J. E. Peralta, G. E. Scuseria, and R. L. Martin, *J. Chem. Phys.* **123**, 174101 (2005).
- [74] M. Shishkin, M. Marsman, and G. Kresse, *Phys. Rev. Lett.* **99**, 246403 (2007).
- [75] N. E. Zein, S. Y. Savrasov, and G. Kotliar, *Phys. Rev. Lett.* **96**, 226403 (2006).
- [76] C. Hartwigsen, S. Goedecker, and J. Hutter, *Phys. Rev. B* **58**, 3641 (1998).
- [77] J. Vandevondele, M. Krack, F. Mohamed, M. Parrinello, T. Chassaing, and J. Hutter, *Comput. Phys. Commun.* **167**, 103 (2005).
- [78] F. Fuchs, J. Furthmüller, F. Bechstedt, M. Shishkin, and G. Kresse, *Phys. Rev. B* **76**, 115109 (2007), [arXiv:0604447 \[cond-mat\]](#).
- [79] K. P. O'Donnell and X. Chen, *Appl. Phys. Lett.* **58**, 2924 (1991).
- [80] M. Shishkin and G. Kresse, *Phys. Rev. B* **75**, 235102 (2007).
- [81] A. L. Kutepov, *Phys. Rev. B* **95**, 195120 (2017).
- [82] G. A. Sawatzky and J. W. Allen, *Phys. Rev. Lett.* **53**, 2339 (1984).
- [83] J. VandeVondele and J. Hutter, *J. Chem. Phys.* **127**, 114105 (2007).
- [84] T. Kotani, M. Van Schilfgaarde, and S. V. Faleev, *Phys. Rev. B* **76**, 165106 (2007), [arXiv:0611002 \[cond-mat\]](#).
- [85] B. E. F. Fender, A. J. Jacobson, and F. A. Wedgwood, *J. Chem. Phys.* **48**, 990 (1968).
- [86] A. K. Cheetham and D. A. O. Hope, *Phys. Rev. B* **27**, 6964 (1983).
- [87] B. Kang and S. Choi, [arXiv:1908.05643](#) (2019), [arXiv:1908.05643](#).
- [88] J. Van Elp, H. Eskes, P. Kuiper, and G. A. Sawatzky, *Phys. Rev. B* **45**, 1612 (1992).
- [89] J. Kuneš, V. I. Anisimov, S. L. Skornyakov, A. V. Lukoyanov, and D. Vollhardt, *Phys. Rev. Lett.* **99**, 156404 (2007).
- [90] I. Leonov, L. Pourovskii, A. Georges, and I. A. Abrikosov, *Phys. Rev. B* **94**, 155135 (2016), [arXiv:1607.08261](#).
- [91] L. Zhang, P. Staar, A. Kozhevnikov, Y. P. Wang, J. Trinastic, T. Schulthess, and H. P. Cheng, *Phys. Rev. B* **100**, 035104 (2019), [arXiv:1705.02387](#).
- [92] T. Chatterji, G. J. McIntyre, and P. A. Lindgard, *Phys. Rev. B* **79**, 172403 (2009).
- [93] R. Zimmermann, P. Steiner, R. Claessen, F. Reinert, S. Hüfner, P. Blaha, and P. Dufek, *J. Phys. Condens. Matter* **11**, 1657 (1999).
- [94] A. Fujimori, M. Saeki, N. Kimizuka, M. Taniguchi, and S. Suga, *Phys. Rev. B* **34**, 7318 (1986).
- [95] J. Kuneš, D. M. Korotin, M. A. Korotin, V. I. Anisimov, and P. Werner, *Phys. Rev. Lett.* **102**, 146402 (2009).
- [96] E. Greenberg, I. Leonov, S. Layek, Z. Konopkova, M. P. Pasternak, L. Dubrovinsky, R. Jeanloz, I. A. Abrikosov, and G. K. Rozenberg, *Phys. Rev. X* **8**, 031059 (2018).
- [97] J. M. Coey and G. A. Sawatzky, *J. Phys. C Solid State Phys.* **4**, 2386 (1971).
- [98] H. Wadati, J. Mravlje, K. Yoshimatsu, H. Kumigashira, M. Oshima, T. Sugiyama, E. Ikenaga, A. Fujimori, A. Georges, A. Radetinac, K. S. Takahashi, M. Kawasaki, and Y. Tokura, *Phys. Rev. B* **90**, 205131 (2014).